processes

MDPI

Article

Choline-Based Ionic Liquids-Incorporated IRMOF-1 for H_2S/CH_4 Capture: Insight from Molecular Dynamics Simulation

Mohamad Adil Iman Ishak [1], Mohd Faisal Taha [1,*], Mohd Dzul Hakim Wirzal [2], Muhammad Najib Nordin [2], Muslim Abdurrahman [3] and Khairulazhar Jumbri [1,*]

1 Department of Fundamental and Applied Sciences and Centre of Research in Ionic Liquids (CORIL), Universiti Teknologi PETRONAS, Seri Iskandar 32610, Perak, Malaysia; mohamad_17008596@utp.edu.my
2 Department of Chemical Engineering, Universiti Teknologi PETRONAS, Seri Iskandar 32610, Perak, Malaysia; mdzulhakim.wirzal@utp.edu.my (M.D.H.W.); najib.nordin23@gmail.com (M.N.N.)
3 Department of Petroleum Engineering, Universitas Islam Riau, Jl. Kaharuddin Nasution, Pekanbaru 28284, Indonesia; muslim@eng.uir.ac.id
* Correspondence: faisalt@utp.edu.my (M.F.T.); khairulazhar.jumbri@utp.edu.my (K.J.); Tel.: +605-368-7843 (K.J.)

Received: 26 November 2019; Accepted: 21 January 2020; Published: 1 April 2020

Abstract: The removal of H_2S and CH_4 from natural gas is crucial as H_2S causes environmental contamination, corrodes the gas stream pipelines, and decreases the feedstock for industrial productions. Many scientific researches have shown that the metal-organic framework (MOF)/ionic liquids (ILs) have great potential as alternative adsorbents to capture H_2S. In this work, molecular dynamics (MD) simulation was carried out to determine the stability of ILs/IRMOF-1 as well as to study the solubility of H_2S and CH_4 gases in this ILs/IRMOF-1 hybrid material. Three choline-based ILs were incorporated into IRMOF-1 with different ratios of 0.4, 0.8, and 1.2% *w*/*w*, respectively, in which the most stable choline-based ILs/IRMOF-1 composite was analysed for H_2S/CH_4 solubility selectivity. Among the three choline-based ILs/IRMOF-1, [Chl] [SCN]/IRMOF-1 shows the most stable incorporation. However, the increment of ILs loaded in the IRMOF-1 significantly reduced the stability of the hybrid due to the crowding effect. Solvation free energy was then computed to determine the solubility of H_2S and CH_4 in the [Chl] [SCN]/IRMOF-1. H_2S showed higher solubility compared to CH_4, where its solubility declined with the increase of choline-based IL loading.

Keywords: ionic liquids; metal-organic framework; hydrogen sulfide; methane; choline; molecular dynamic

1. Introduction

Hydrogen sulphide (H_2S) is a highly toxic, colourless, flammable gas with a pungent odour. It is a gas that is often produced in the processing of crude oil and natural gases as it occurs in the subsurface as free gas and in oil due to its high solubility. H_2S is also a by-product of the breakdown of organic waste as well as other industrial processes. It is significant to perform the removal of H_2S as it causes operational problems in both oil and gas industries. It is highly corrosive to pipeline throughout the production facilities [1], leading to an economical deleterious effect because a washing plant is required to remove H_2S in order to prevent corrosion and render the residual gas safe for domestic combustion. H_2S also has adverse effects on the environment and human health. Exposure to high concentrations of H_2S is extremely hazardous and can be fatal. Thus, the reduction of H_2S emission becomes one of the main interests [2], especially in the biogas, syngas, and natural gas purification processes [3,4].

For the past decades, amine gas has been commonly used as a treating agent to separate H_2S from natural gas in oil and gas industries. Single and binary mixtures of alkanolamines, such as diethanolamine (DEA), monoethanolamine (MEA), *N*-methyldiethanolamine (MDEA), and di-isopropanolamine (DIPA), are commonly used as the treating agents to remove H_2S and CO_2 from natural gas [5]. However, it is necessary to find an alternative technique that is cleaner, with low energy consumption and cost, and at the same time is able to maintain or increase the production rate. The use of single and binary mixtures of alkanolamines as treating agents for the removal of H_2S have some drawbacks in terms of performance and efficiency. Among them are the degradation of alkanolamine, the production of a corrosive side product due to oxidation reaction, and loss of alkanolamine inside the gas stream [6]. Plus, energy demand for the process is huge due to the wide energy gap on the reaction between the acid gases and alkanolamines, as well as the use of water as a solvent, which exhibits high heat capacity [7].

Ionic liquids (ILs) are currently used as a new technology to separate H_2S from natural gases due to their high thermal stability, low volatility [8], and alteration of their functionalized group [9,10]. ILs are made up of cation and anion that exist in the form of molten salt or liquid with a melting point below 100 °C [11] or close to the ambient condition [12]. Due to these fascinating properties, ILs are widely used as solvents in numerous applications, including gas adsorption [13,14], catalysis and extraction [12,15], batteries and electrolyte [16–18], and molecular sensors [19]. Previous studies reveal the efficiency and capability of ILs to absorb H_2S with numerous modifications and improvement. As the solubility of H_2S in ILs is highly dependent on the partial pressure of H_2S, most ILs can be classified as "physical" solvents and operated efficiently in the presence of H_2S under high partial pressure and high concentration [20]. It has been reported that ILs with moderate basicity demonstrated better selectivity because the strong alkali groups interact excellently with H_2S, making ILs a promising aspirant to separate H_2S from other gases, such CO_2 and CH_4.

Huang et al. [21] studied the performance of H_2S absorption by using 1-alkyl-3-methylimidazolium carboxylate ILs at different temperatures, where the absorption capacities of H_2S intensified compared to other common ILs. This is due to the alkalinity of the anions and also a small contribution from the alkyl chain lengths of the cations. Meanwhile, 1-hexyl-3-methylimidazolium chloride has been effectively used for the capture and conversion of H_2S by using the Claus reaction, where H_2S was converted to S_8 in a high conversion ratio by more than 96% in just 3 min [10]. Imidazolium-based ILs are widely used as liquid solvent for numerous applications, since they demonstrate excellent performance in gas adsorption and separation. However, the toxicity of imidazolium-based ILs has opened a new path towards finding a safe and environmentally-friendly IL. One of these paths are choline-based ILs, which have high a potential for practical use, since they are highly biodegradable and cost-effective. However, the efficiency of choline-based ILs in gas separation are hindered due to their high viscosity. Supporting ILs (SILs) are one of the promising solutions that are able to reduce the viscosity of ILs, thus improving the adsorption efficiency. The introduction of a metal-organic framework (MOF) as a support material will help in the immobilization of ILs, as they are dispersed all over the surface while preserving the unique properties of the MOF itself. In this concept, immobilization of ILs inside the MOF will reduce the strong association of ions, which contributes to their high viscosity, where the ions will be tethered on the solid surface. Therefore, SILs will be beneficial to both the MOF and ILs by improving the functionality and selectivity of the MOF towards gases, reducing the usage of ILs depending on the loading ratio, as well as increasing the gas solubility due to the presence of active sites.

MOF appears as one of the best materials to be used as the supporting absorber due to its intriguing features, such as high surface contact, high porosity [22–26] and pore volume, large gas storage, and high tunability [27–29], making it a suitable material for gas separation and adsorption. It is widely used in gas separation and storage [30–32], ion exchange [33,34], catalysis, and conductivity [35,36]. The MOF has been proposed as a SIL to improve the separation efficiency and enhance the physical nature of ILs by reducing the viscosity and increasing the gas solubility. The integration of both the MOF

and ILs into a hybrid will reinforce the adsorption efficiency and, consequently, raise the H_2S uptake. The proportion of ILs should be taken into consideration, since the adsorption capacity is affected by this factor. For example, the adsorption of a sulphurous compound (BT) was unsatisfactory with 33% loading of BMIM-Cl into MIL-101 [37]. This was due to the fulfilment of pore sites with BMIM-Cl in the MOF that hinder the adsorption availability. A similar observation was reported by Qiao et al. [38], where the adsorption of CO_2 was reduced by the addition of the amine group inside the MOF due to the unavailability of free pore volume. Selection of the MOF should be focussed on its ability to capture a high volume of guest molecules and on the selectivity of the desired guest molecules. Zheng et al. [39] stated that the design and synthesis of flexible MOFs, which can interact with certain guest molecules in a switchable way, would be appealing to explore. Furthermore, Abroshan and Kim [40] studied the stability of IRMOF-1 and IRMOF-10 after the incorporation of imidazolium and pyridinium-based ILs by molecular dynamics. They found that both IRMOF-1s are stable at low ILs loading but eventually collapse and deform at high IL loading, specifically at 15 ion pairs. Moreover, the stability of the IRMOFs is governed by the selection of different ILs, since each type contributes various stabilities towards the framework. Furthermore, Gupta et al. [41] conducted a simulation study on the adsorption of CO_2/N_2 gas mixture inside the IL/IRMOF-1, where the CO_2 showed dominant interaction towards the anions. Meanwhile, Li et al. [42] computationally studied the solubility of H_2S and CH_4 in IL/MOF composite using four types of imidazolium-based ILs, where Cu-TPDPAT was used as the MOF. It showed that the adsorption of H_2S and its selectivity over CH_4 was improved upon IL loading compared to pristine Cu-TDPAT, in which the anion interacts dominantly with the gas compared to cation.

At present, computational study is utilised as a complement to experimental findings because it provides a detailed interaction and dynamic properties of the proposed study. Therefore, molecular dynamics (MD) simulation was conducted to provide an insight on the interaction, where IRMOF-1 was chosen as a potential MOF due to its high surface area and pore volume compared to other kinds of MOFs, specifically the zeolitic imidazolate framework (ZIF) and Cu-BTC. These remarkable properties help in providing a wide medium and capacity for gas accommodation. Meanwhile, choline-based ILs were selected as potential solvents due to their biodegradable, biocompatibility, and cost-effective qualities, compared to other common ILs. The combination of IRMOF-1 and choline-based ILs as a hybrid material will not only improve the gas adsorption performance but also promote the environmentally-friendly aspect, compared to common imidazolium and pyridinium-based IL/MOF. This work focussed on the prediction towards the stability of the IL/IRMOF-1 composite upon ILs incorporation, as well as the solubility of H_2S and CH_4 inside the hybrid composite.

2. Simulation Details

2.1. Incorporation of Choline-Based ILs İnside IRMOF-1

Choline methyl sulphate ([Chl][$MeSO_4$]), choline thiocyanate ([Chl][SCN]), and choline triflate ([Chl][TfO]) (see Figure 1) were packed inside the IRMOF-1 structure by using PyMOL. IRMOF-1 was obtained from the ChemTube 3D, originating from University of Liverpool [43]. The IRMOF-1 framework was built up by coordination of four oxide zinc atoms bonded to six carboxylate benzene rings in the subsequent arrangement to form a uniform porous pore. The optimized potential of liquid simulations (OPLS) force field was used, and the force field parameters were obtained from Chen et al., [44]. A Berendsen thermostat and Berendsen barostat were used for temperature and pressure control, respectively, in which the temperature was set up at 298 K, while the pressure was at 1 atm. A 2.6 × 2.6 × 2.6 nm cubic box was used to create the initial system of choline-based ILs/IRMOF-1. The IRMOF-1 was placed at the centre of the box and incorporated with three different weight percentages ($W_{ILs/IRMOF1}$ 0.4, 0.8, and 1.2%). Table 1 shows the number of ILs with respect to its ratios. For example, 14, 27, and 41 ion pairs of [Chl][SCN] were infused inside the IRMOF-1, where each number of ions pairs corresponded to a 0.4, 0.8, and 1.2% IL ratio. In this work, only one

subunit of IRMOF-1 was used. The choline-based ILs and IRMOF-1 were packed together by using Packmol. Energy minimization was the first step in the simulation flow. In this step, there were two main algorithms; the steepest descent and the conjugate gradient scheme. A total of 100,000 steps were applied with a time step of 0.2 fs for each minimization step. This step was carried out to optimize the orientation of IL molecules in the system. The pre-production NVT run was applied for proper pre-equilibrium as final checking before the real simulation. The production simulation was performed in a conical ensemble (NPT) for 50 ns.

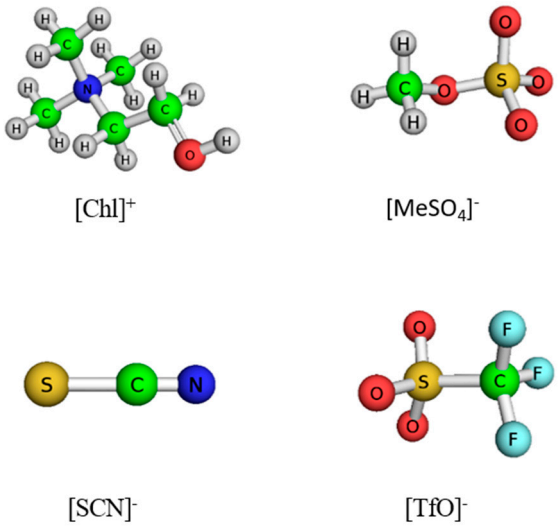

Figure 1. Molecular structures of cation $[Chl]^+$ and three anions ($[MeSO_4]$, [SCN], and $[TfO]^-$) of ionic liquids (ILs) to be incorporated inside IRMOF-1.

Table 1. The number of ILs inside the choline-based ILs/IRMOF-1 with different weight ratios.

No	System	Choline-Based IL: IRMOF-1 Ratio (*w*/*w*%)		
		0.4	**0.8**	**1.2**
1	$[Chl][MeSO_4]$	9	21	31
2	[Chl][SCN]	14	27	41
3	[Chl][TfO]	9	17	26

2.2. Solvation Free Energy

Solubility of H_2S and CH_4 was predicted through solvation free energy simulation and calculation was done by using the Bennet acceptance ratio (BAR) method. Solvation free energy was computed with the same parameters and conditions as in the choline-based ILs/IRMOF-1 with an additional free energy parameter. A total of 21 sets of λ were used, starting from $\lambda = 0$ to $\lambda = 1$, with a total of 5 ns of simulation time for each λ. The energy of the systems was minimized using the steepest descent, followed by the conjugate gradient, with a total of 5000 steps for each algorithm. Then, the system was continued at 298 K and 1.0 bar for 100 ps in NVT, followed by 5 ns in NPT. The free energy difference between two states, *i* and *j*, was calculated using Equation (1), adopted from Bennett [45], where k_B and T are the Boltzmann constant and temperature, respectively. Both H_i and H_j denoted the Hamiltonians at states *i* and *j*, while *C* was determined in repetition in order to satisfy the $f(H_i - H_j + C)_j = f(H_i - H_j - C)_i$ condition. The f function was denoted from the Fermi function, as shown in Equation (2).

$$\Delta G_{ji}^{BAR} = k_B T \left(ln \frac{f\left(H_i - H_j + C\right)j}{f(H_i - H_j - C)i} \right) + C \quad (1)$$

$$f(x) = \frac{1}{1 + \exp\left(\frac{x}{k_B T}\right)} \tag{2}$$

The free energy difference was calculated from Equations (3) and (4),

$$\Delta G_{ji}^{BAR} = -k_B T \, ln \frac{N_j}{N_i} + C \tag{3}$$

$$\Delta G_{BA}^{BAR} = \sum_{i=1}^{n-1} \Delta G_{i+1,i}^{BAR}, \tag{4}$$

where N_j and N_i indicate the number of coordinate frames at λ_i and λ_j, respectively. Technically, the forward (FW) and backward (BW) energy differences should be overlapped adequately to achieve the convergence of this process, which is the crucial aspect for the BAR method [45]. The data would then be reliable if the overlap integral relied minimally on 0.01, as proposed by Bruckner and Boresch [46], in which the overlapping could be observed from the normalized histograms of the energy differences. Otherwise, the repetition of the process would not be converged or unreliable data would be generated due to the insufficient overlap.

$$\Delta U_l^{FW} = U(\lambda_{l+1}) - U(\lambda_l)\big|_{\lambda_l} \tag{5}$$

$$\Delta U_{l+1}^{BW} = U(\lambda_l) - U(\lambda_{l+1})\big|_{\lambda_l} \tag{6}$$

In Equations (5) and (6), the λ symbol represents the λ-value once the trajectory is generated. The overlap could be detected by overlaying the histograms from both Equations (5) and (6) with respect to the $\Delta {U_l}^{FW}$ and $\Delta {U_{l+1}}^{BW}$ values. However, the actual amount of overlap cannot be obtained directly through the visual inspection. Hence, the overlap integral ${OI_{l,l+1}}^{BAR}$ was introduced as the numerical guide to provide the proper point for improvement in the existing free energy protocol. The interval λ_l, λ_{l+1} is formulated as Equation (7), where $h_b(X)$ represents the normalized histogram of quantity X with a total number of B bins. The non-zero value of ${OI_{l,l+1}}^{BAR}$ was contributed from the configuration in the overlap zone, in which 0 indicates that there is no overlap zone, while 1 represents a perfect overlap.

$$OI_{l,l+1}^{BAR} = 2 \cdot \sum_{b=1}^{B} \frac{h_b\left(\Delta U_l^{FW}\right) \cdot h_b\left(\Delta U_{l+1}^{BW}\right)}{h_b\left(\Delta U_l^{FW}\right) + h_b\left(\Delta U_{l+1}^{BW}\right)} \tag{7}$$

The solubility of each gas is calculated using Equation (8) [47].

$$\mathrm{S} = \frac{1}{RT} exp\left(-\frac{\Delta G_{sol}}{RT}\right) \tag{8}$$

3. Results and Discussion

3.1. Stability of ILs/IRMOF-1

After the incorporation of choline-based ILs into IRMOF-1, the root mean square deviation (RMSD) was calculated to determine the stability and sustainability of choline-based IL/IRMOF-1 composites. Table 2 shows the RMSD value for ILs/IRMOF-1 at three different weight ratios. IRMOF-1 is well known for its fragility and poor stability in the aqueous phase, where it tends to collapse upon contact with water [48]. With the presence of water molecules in pristine IRMOF-1, the calculated RMSD was 1.423 nm at 298 K. This high deviation justified the instability of IRMOF-1, but upon incorporation of ILs inside the IRMOF-1, its stability significantly improved by preventing direct contact with water. Therefore, it can be deduced that the incorporation of ILs inside the IRMOF-1 caused some modification in molecular structure from the original state.

Table 2. Root mean square deviation (RMSD) value of choline-based ILs/IRMOF-1 at different weight ratios, simulated at 298 K and 1 atm.

Entry	System	Choline-Based ILs: IRMOF-1 Ratio (*w*/*w*%)			
		0.4	**0.8**	**1.2**	**-**
1	[Chl][$MeSO_4$]	0.805 ± 0.044	0.844 ± 0.037	1.040 ± 0.041	-
2	[Chl][SCN]	0.674 ± 0.041	0.983 ± 0.022	1.280 ± 0.021	-
3	[Chl][TfO]	0.767 ± 0.038	0.900 ± 0.031	0.945 ± 0.034	-
4	Water	-	-	-	1.423 ± 0.049

Based on Table 2, [Chl][SCN]:IRMOF-1 at 0.4% *w*/*w* displayed the lowest deviation with a RMSD value of 0.674 nm. In the same ratio, [Chl][TfO] and [Chl][$MeSO_4$] showed a slightly higher RMSD value of 0.767 nm and 0.805 nm, respectively. This result suggests that the selection of anion in choline-based ILs plays an important role in quantifying the stability of IRMOF-1.

Furthermore, the size of anions was also one of the main factors affecting the stability of the composite. The size of the anion decreased in the order of $[SCN]^-$ < $[TfO]^-$ < $[MeSO_4]^-$. This indicates that a smaller anion contributed to a better stability compared to a bulky anion. The smaller anion could penetrate and diffuse easily inside the pores of IRMOF-1, and, as a result, could scatter in a better dispersion. This promotes IRMOF-1 to gain a stronger interionic interaction towards [Chl][SCN], compared to the other two choline-based ILs. Therefore, the enhancement of this interionic interaction helped in supporting the IRMOF-1 structure from being collapsed as it was tightly held by [Chl][SCN].

Moreover, the stability of the hybrid material varied, according to the number of ILs inside the IRMOF-1. Based on Table 2, the calculated RMSD value increased as the weight percentage of ILs multiplied. This result indicates that a small number of ILs was sufficient to maintain the stability of the composite. This phenomenon could be explained as follows: By increasing the number of ILs inside the MOF, the excess number of ILs created a crowding effect which hindered the interionic interaction of the attractive ions towards the IRMOF-1. Consequently, the interaction between choline-based ILs and the IRMOF-1 deteriorated, thus reducing the stability of the choline-based ILs/IRMOF-1.

3.2. Interaction of Choline-Based ILs İnside the IRMOF-1

From the RMSD value, the infusion of choline-based ILs inside the IRMOF-1 affected the stability of the framework, in which the interaction of the cation and anion of the ILs also varied upon their incorporation. In order to quantify the interaction between the anion and cation inside the IRMOF-1 framework, the radial distribution function (RDF) was plotted, as shown in Figure 2. The interaction of the opposite ions observed was lower in the bulk phase, as shown in Figure 2a, compared to the hybrid materials phase. Meanwhile, their interaction significantly increased inside the IRMOF-1 framework, in which the highest interaction between opposite ions was exhibited by 0.4% *w*/*w* ([Chl][SCN]/IRMOF-1) loading. The strong interaction could be explained by the confinement effect being posed by the IRMOF-1 framework, in which the ions inside the framework were packed closely together. In addition, the different charges posed by $[Chl]^+$ and $[SCN]^-$ promoted strong electrostatic forces, as can be seen by the red peak in Figure 2a.

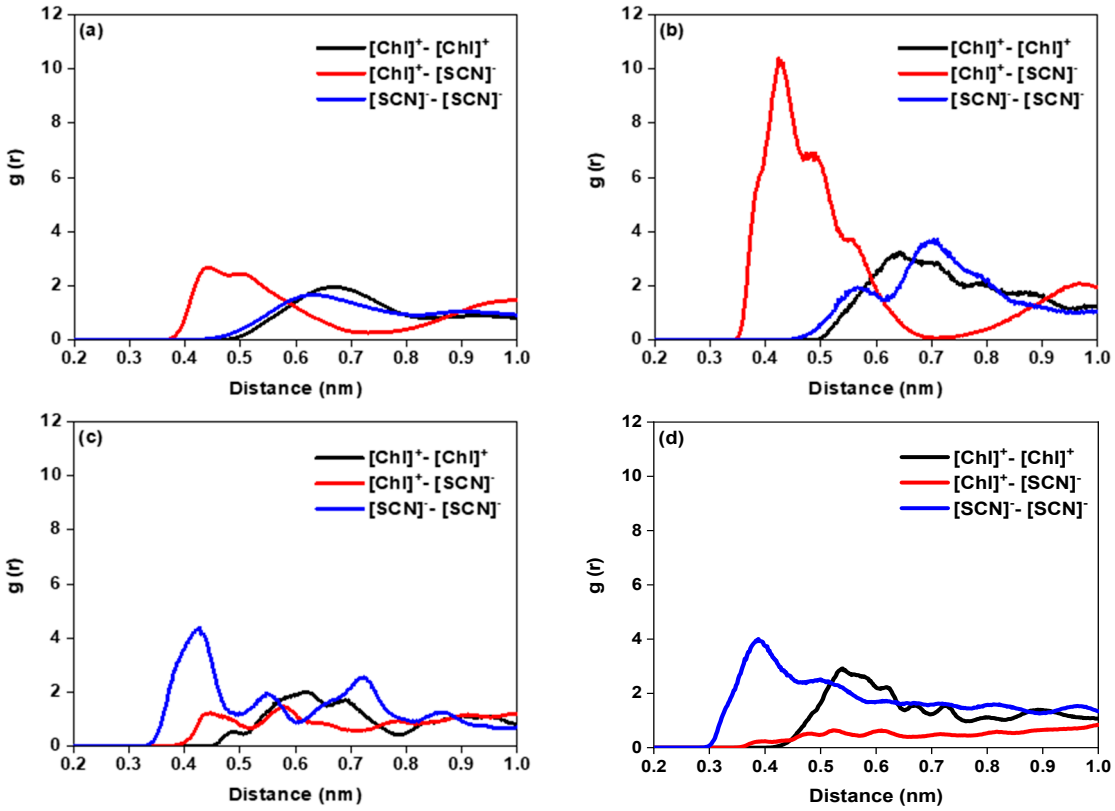

Figure 2. Radial distribution function (RDF) of [Chl]+ and [SCN]− in (**a**) the bulk phase, (**b**) 0.4% *w*/*w*, (**c**) 0.8% *w*/*w*, and (**d**) 1.2% *w*/*w* of IL loading in [Chl][SCN]/IRMOF-1 composites at 298 K and 1 atm.

In contrast, both $[Chl]^+$-$[Chl]^+$ and $[SCN]^-$-$[SCN]^-$ showed unfavourable interaction, since they repelled each other due to their identical charges. It can be seen that the $[Chl]^+$-$[SCN]^-$ interaction showed the highest peak intensity at 0.4% *w*/*w* loading with the shortest distance of 0.45 nm, but the peak intensity declined at 0.8% *w*/*w* and further decreased at 1.2% *w*/*w*, as shown in Figure 2b–d, respectively. This observation could be due to the crowding effect of the IL ions. Meanwhile, the interaction of $[SCN]^-$-$[SCN]^-$ was higher in both 0.8% *w*/*w* and 1.2% *w*/*w* with the 0.4 nm distance of interaction. This was because $[SCN]^-$ was able to penetrate and move around easily inside the pores of IRMOF-1 due to its small size, making it easier to interact. Furthermore, the bulky size of $[Chl]^+$ hindered it to interact with $[SCN]^-$ inside the pores. Figure 3 illustrates the snapshot of [Chl][SCN] packed inside the IRMOF-1, which shows the crowding effect by [Chl][SCN] at a high percentage of ILs (refer to Figure 3b,c). The accumulation of $[Chl]^+$ and $[SCN]^-$ ions inside the IRMOF-1 framework with various IL loadings was inspected in 2D visualisation by mapping through the density map taken from the z-axis direction, as shown in Figure 4. It can be observed that the pore volume of IRMOF-1 was fully occupied by $[Chl]^+$ as it was larger in size compared to $[SCN]^-$ (Figure 4b). As shown by Figure 4c, a low density of $[SCN]^-$ accumulated inside the pore due to its small size.

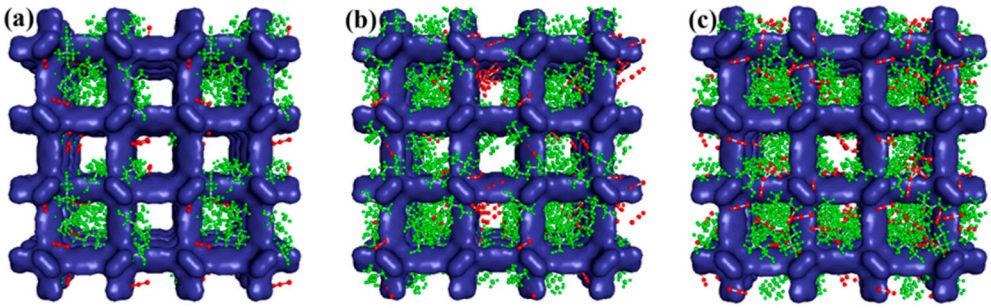

Figure 3. Snapshot of $[Chl]^+$ and $[SCN]^-$ packed inside IRMOF-1 at (**a**) 0.4% *w*/*w*, (**b**) 0.8% *w*/*w*, and (**c**) 1.2% *w*/*w* of IL loading at 298 K and 1 atm. Colour code: IRMOF-1 (blue); $[Chl]^+$ (green); $[SCN]^-$ (red).

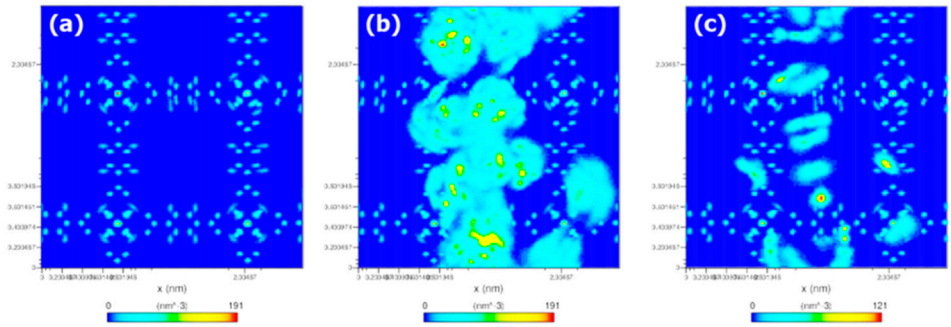

Figure 4. Density map of (**a**) IRMOF-1, (**b**) $[Chl]^+$, and (**c**) $[SCN]^-$ distributed inside the pore volume.

3.3. Solubility and Solubility Selectivity of H_2S/CH_4 Inside [Chl][SCN]/IRMOF-1

The solubility of H_2S and CH_4 inside the [Chl][SCN]/IRMOF-1 was calculated from the solvation free energy. Table 3 shows the excess chemical potential (μ^{ex}) and calculated solubility of each gas inside the hybrid material for three different loadings of [Chl][SCN]. The solubility rate of the gases was quantified by the value of μ^{ex}, in which the solubility of each gas intensified as the negative value of μ^{ex} increased. Based on Table 3, H_2S and CH_4 in the pure ILs and IRMOF-1 exhibited lower solubility compared to those in IL/IRMOF-1 composites, respectively. The μ^{ex} value of H_2S inside the pristine IRMOF-1 was 0.122 kcal/mol, suggesting its poor solubility. This indicates that IRMOF-1 had a weak interaction with H_2S, which reflects its low affinity and selectivity in capturing gas. As for the pure ILs, we predict that the viscosity was the limitation for the gas solubility. This is because viscous IL possesses strong association between its anion and cation, which will hinder interaction with gases. Meanwhile, H_2S and CH_4 showed a negative value of μ^{ex} in IL/IRMOF-1, which indicates that both gases were soluble in the composite. However, H_2S dominated in the solubility compared to CH_4 where the μ^{ex} value was more negative for all [Chl][SCN] loadings. This could be explained according to the "like dissolve like" principle, in which H_2S "dissolves" faster in the [Chl][SCN]/IRMOF-1 composite due to the highly polar nature of [Chl][SCN] towards H_2S with the presence of the permanent dipole moment on H_2S [49]. On the other hand, the interaction of this IL with CH_4 molecules qwas less favourable compared to H_2S, due to the non-polarizability of CH_4 [50].

Table 3. Excess chemical potential (μ^{ex}), solubility (S), and solubility selectivity (SS) of H_2S and CH_4 inside the [Chl][SCN]/IRMOF-1 composite, comprising of different IL loadings at 298 K and 1 atm.

System	μ^{ex} (H_2S) (kcal/mol)	μ^{ex} (CH_4) (kcal/mol)	S_{H_2S} (mol L^{-1} bar^{-1})	S_{CH_4} (mol L^{-1} bar^{-1})	SS_{H_2S/CH_4}
Pure IL	−0.349 (0.028)	−0.012 (0.022)	0.073 (0.006)	0.041 (0.027)	1.780 (0.664)
IRMOF-1	0.122 (0.034)	−0.153 (0.004)	0.033 (0.009)	0.052 (0.001)	0.635 (0.273)
IL-MOF (14 IL)	−1.109 (0.032)	−0.103 (0.009)	0.263 (0.007)	0.048 (0.004)	5.479 (0.087)
IL-MOF (27 IL)	−1.104 (0.038)	−0.122 (0.014)	0.260 (0.009)	0.050 (0.006)	5.200 (0.125)
IL-MOF (41 IL)	−0.966 (0.034)	−0.153 (0.018)	0.206 (0.007)	0.052 (0.006)	3.962 (0.120)

The solubility of H_2S decreased as the [Chl][SCN] loadings multiplied, where the μ^{ex} value increased from −1.109 until −0.966 kcal/mol for each loading of [Chl][SCN]. The greater the quantity of $[Chl]^+$ and $[SCN]^-$ accommodated inside the IRMOF-1 framework, the lesser the amount of H_2S molecules to interact, and, hence, this reflects its lower solubility. However, the solubility of CH_4 inside [Chl][SCN]/IRMOF-1 showed the opposite trend. The increased number of $[Chl]^+$ and $[SCN]^-$ significantly strengthened the interaction with CH_4 molecules. This observation might be explained by the nonpolar−nonpolar dispersive interactions due to the addition of nonpolar alkyl-chains from $[Chl]^+$ [51].

In order to determine the binding and interaction of each gas toward $[Chl]^+$ and $[SCN]^-$ inside the IRMOF-1, the RDF was plotted. Figure 5 shows the RDF of H_2S and CH_4 towards $[Chl]^+$ and $[SCN]^-$ inside the IRMOF-1 with various loadings of [Chl][SCN] at 298 K and 1 atm. It was found that H_2S favourably interacted with IL, as can be seen from the intensity of the peak which was significantly higher for all [Chl][SCN] loadings. However, the interaction of H_2S towards IL gradually reduced with the increase of [Chl][SCN] loading, as shown in Figure 5a, where the peak intensity decreased for both H_2S-$[Chl]^+$ and H_2S-$[SCN]^-$. The interaction of CH_4-$[Chl]^+$ and CH_4-$[SCN]^-$ was amplified following the increment in [Chl][SCN] loading inside the IRMOF-1, as shown in Figure 5b.

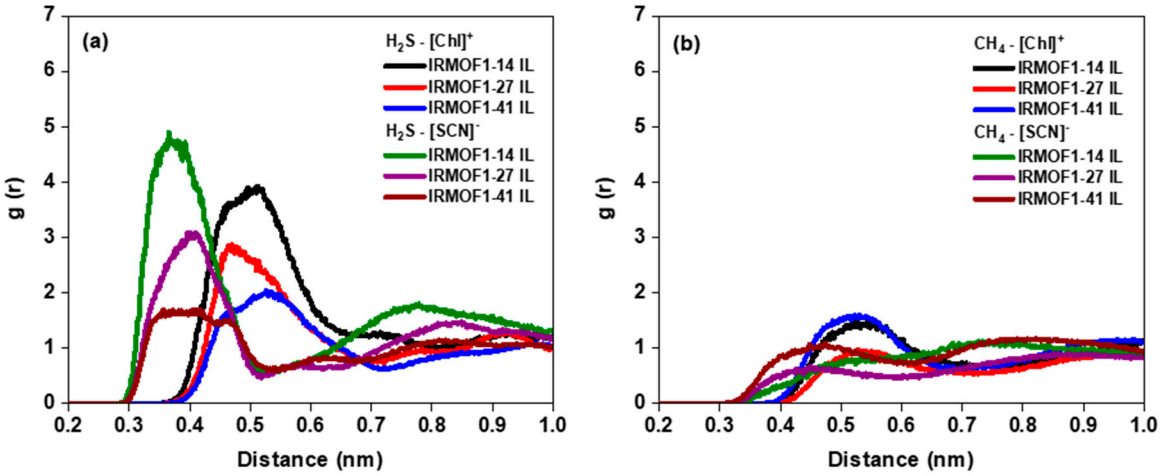

Figure 5. Radial distribution function of (**a**) H_2S and (**b**) CH_4 interaction towards [Chl][SCN]/IRMOF-1 composite.

In terms of specific ions interaction, H_2S attracted more towards $[SCN]^-$ at 14 IL loading (0.4% *w*/*w*), whereas CH_4 preferably interacted with $[Chl]^+$, specifically at 41 IL loading (1.2% *w*/*w*). However,

the interaction of the gases favored towards $[SCN]^-$, as was observed from the intensity of the peak, which indicates that the anion played a significant role in gas adsorption. The small size of $[SCN]^-$ allowed greater adsorption sites for gases compared to the bulkier size of $[Chl]^+$.

3.4. Solubility of H_2S and CH_4 Inside the IL/IRMOF-1 Composite

The effect of temperature on the gas solubility inside the [Chl][SCN]/IRMOF-1 composite was further analysed. [Chl][SCN] was chosen due to its stability upon integration with MOF. Solvation free energy was computed for various [Chl][SCN] loadings as the temperature varied. Table 4 shows the μ^{ex} and calculated solubility (S) of H_2S and CH_4 inside the [Chl][SCN]/IRMOF-1 at 303, 313, 323, and 333 K. As the temperature elevated, the solubility of H_2S and CH_4 inside the [Chl][SCN]/IRMOF-1 decreased for each [Chl][SCN] loading. The relationship between temperature and solubility of H_2S in this work shows a similar trend with the previous study [52]. The highest solubility of H_2S was observed at 303 K with the μ^{ex} value of −1.116 kcal mol^{-1} and 0.266 mol L^{-1} bar^{-1} at 14 IL (0.4% *w*/*w*) loading.

Table 4. Excess chemical potential (μ^{ex}) and solubility (S) of H_2S and CH_4 inside the [Chl][SCN]/IRMOF-1 composite, comprising of different IL loadings at 303, 313, 323, and 333 K.

System	μ^{ex} (H_2S) (kcal/mol)	μ^{ex} (CH_4) (kcal/mol)	S_{H_2S} (mol L^{-1} bar^{-1})	S_{CH_4} (mol L^{-1} bar^{-1})
		303 K		
MOF5-14 IL	−1.116 (0.025)	−0.122 (0.008)	0.266 (0.006)	0.050 (0.003)
MOF5-27 IL	−1.042 (0.034)	−0.122 (0.017)	0.235 (0.008)	0.050 (0.007)
MOF5-41 IL	−1.023 (0.049)	−0.172 (0.016)	0.227 (0.011)	0.054 (0.005)
		313 K		
MOF5-14 IL	−0.966 (0.029)	−0.115 (0.007)	0.206 (0.006)	0.049 (0.003)
MOF5-27 IL	−0.985 (0.038)	−0.117 (0.013)	0.213 (0.008)	0.049 (0.005)
MOF5-41 IL	−0.918 (0.039)	−0.160 (0.021)	0.190 (0.008)	0.053 (0.007)
		323 K		
MOF5-14 IL	−0.813 (0.027)	−0.103 (0.009)	0.159 (0.005)	0.048 (0.004)
MOF5-27 IL	−0.939 (0.027)	−0.074 (0.013)	0.197 (0.006)	0.046 (0.008)
MOF5-41 IL	−1.004 (0.039)	−0.141 (0.022)	0.220 (0.009)	0.051 (0.008)
		333 K		
MOF5-14 IL	−0.899 (0.033)	−0.112 (0.006)	0.184 (0.007)	0.049 (0.003)
MOF5-27 IL	−0.930 (0.038)	−0.086 (0.012)	0.194 (0.008)	0.047 (0.006)
MOF5-41 IL	−0.851 (0.035)	−0.108 (0.017)	0.170 (0.007)	0.048 (0.008)

Furthermore, the calculated solubility of H_2S at 14 IL (0.4% *w*/*w*) loading decreased from 0.266 to 0.184 mol L^{-1} bar^{-1} at 298 K and 333 K, respectively. This trend was similar to 27 IL (0.8% *w*/*w*) and 41 IL (1.2% *w*/*w*) loading for both H_2S and CH_4. Since anions contributed a major effect towards the solubility of the gas [42,53], the rise in temperature significantly affected the interaction between anions and gases. The decline in gas solubility as the temperature rose could be explained from the weakening of the bonding in the intermolecular interaction between IL and gas. This is because $[SCN]^-$ existed as a conjugate base and acted as a hydrogen-bond acceptor [54]. Therefore, $[SCN]^-$ was able to form hydrogen bonding with the gases, which in turn allowed the gases, especially H_2S, to solubilise [55]. However, the increase in temperature weakened the bonding and reduced the intermolecular interaction of IL-gas. This is in agreement with other experimental works [56,57].

4. Conclusions

In conclusion, the stability of the choline-based ILs/IRMOF-1 composite was successfully predicted by MD simulation. [Chl][SCN] was found to be the best choline-based IL to incorporate inside the IRMOF-1, compared to $[Chl][MeSO_4]$ and [Chl][TfO], since it displayed a high stability as a hybrid

composite with the lowest RMSD value (0.674 ± 0.041 nm) at a 0.4% *w*/*w* ratio. Different charges of $[Chl]^+$ and $[SCN]^-$ allowed favorable interaction between them, where the intermolecular interaction was much higher in the [Chl][SCN]/IRMOF-1 composite compared to the bulk [Chl][SCN] due to a confinement effect of the IRMOF-1 framework, as proven by RDF. For the solubility study, H_2S adsorbed excellently inside [Chl][SCN]/IRMOF-1 compared to CH_4. Anion showed significant contribution towards the solubility of H_2S, where H_2S-$[SCN]^-$ interaction was favorable compared to H_2S-$[Chl]^+$. Due to the presence of nonpolar−nonpolar interaction, CH_4 was more attracted towards $[Chl]^+$, where the solubility of the gas improved with the increment of [Chl][SCN] loading. Meanwhile, at a greater [Chl][SCN] loading, the excess amount of IL hindered the H_2S to form an interaction towards $[SCN]^-$, hence the reduce in solubility. Moreover, the solubility of H_2S and CH_4 inside IL/IRMOF-1 decreased due to the weakening of their bonding as the temperature elevated.

Author Contributions: Conceptualization, M.F.T., K.J., and M.D.H.W.; methodology, K.J. and M.D.H.W.; software, K.J.; validation, M.F.T., M.A.I.I., and M.N.N.; formal analysis, M.A.I.I. and M.N.N.; investigation M.A.I.I., M.N.N., and M.F.T.; resources, K.J., M.F.T., and M.A.; writing—original draft preparation, M.A.I.I. and M.N.N.; writing—review and editing, K.J., M.F.T., M.D.H.W., and M.A.; visualization, K.J., M.F.T., M.A.I.I., and M.N.N.; supervision, K.J., M.F.T., and M.D.H.W.; funding acquisition, K.J. and M.A. All authors have read and agreed to the published version of the manuscript.

Funding: This research was funded by the UTP-UIR International Grant (015ME0-040).

Acknowledgments: The authors would like to acknowledge Universiti Teknologi PETRONAS (UTP) and Universiti Islam Riau (UIR) for providing the research grant.

Conflicts of Interest: The authors declare no conflict of interest.

References

1. Ge, K.; Wu, Y.; Wang, T.; Wu, J. Humidity swing adsorption of H_2S by fibrous polymeric ionic liquids (PILs). *Sep. Purif. Technol.* **2019**, *217*, 1–7. [CrossRef]
2. Seoane, B.; Coronas, J.; Gascon, I.; Etxeberria Benavides, M.; Karvan, O.; Caro, J.; Kapteijn, F.; Gascon, J. Metal-organic framework based mixed matrix membranes: A solution for highly efficient CO_2 capture? *Chem. Soc. Rev.* **2015**, *44*, 2421–2454. [CrossRef] [PubMed]
3. Yang, L.; Ge, X.; Wan, C.; Yu, F.; Li, Y. Progress and perspectives in converting biogas to transportation fuels. *Renew. Sustain. Ener. Rev.* **2014**, *40*, 1133–1152. [CrossRef]
4. Faramawy, S.; Zaki, T.; Sakr, A.A.E. Natural gas origin, composition, and processing: A review. *Nat. Gas Sci. Eng.* **2016**, *34*, 34–54. [CrossRef]
5. El-Bishtawi, R.; Haimour, N.M. Claus recycle with double combustion process. *Fuel Process. Technol.* **2004**, *86*, 245–260. [CrossRef]
6. Galán Sánchez, L.M.; Meindersma, G.W.; de Haan, A.B. Solvent Properties of Functionalized Ionic Liquids for CO_2 Absorption. *Chem. Eng. Res. Des.* **2007**, *85*, 31–39. [CrossRef]
7. Camper, D.; Bara, J.E.; Gin, D.L.; Noble, R.D. Room-Temperature Ionic Liquid-Amine Solutions: Tunable Solvents for Efficient and Reversible Capture of CO_2. *Ind. Eng. Chem. Res.* **2008**, *47*, 8496–8498. [CrossRef]
8. Greer, A.J.; Taylor, S.F.R.; Daly, H.; Quesne, M.; Catlow, C.R.A.; Jacquemin, J.; Hardacre, C. Investigating the Effect of NO on the Capture of CO_2 Using Superbase Ionic Liquids for Flue Gas Applications. *ACS Sust. Chem. Eng.* **2019**, *7*, 3567–3574. [CrossRef]
9. Yunqian, M.; Jiaming, M.; Cong, X.; Yan, L.; Lihua, Z. Immobilization of Functionalized Ionic Liquid on Sol-Gel Derived Silica for Efficient Removal of H_2S. *China Petro. Process. Petrochem. Technol.* **2019**, *21*, 62–70.
10. Huang, K.; Feng, X.; Zhang, X.-M.; Wu, Y.-T.; Hu, X.-B. The ionic liquid-mediated Claus reaction: A highly efficient capture and conversion of hydrogen sulfide. *Green Chem.* **2016**, *18*, 1859–1863. [CrossRef]
11. De Riva, J.; Ferro, V.R.; del Olmo, L.; Ruiz, E.; Lopez, R.; Palomar, J. Statistical Refinement and Fitting of Experimental Viscosity-to-Temperature Data in Ionic Liquids. *Ind. Eng. Chem. Res.* **2014**, *53*, 10475–10484. [CrossRef]
12. Hallett, J.P.; Welton, T. Room-temperature ionic liquids: Solvents for synthesis and catalysis. 2. *Chem. Rev.* **2011**, *111*, 3508–3576. [CrossRef] [PubMed]

13. Abedini, A.; Crabtree, E.; Bara, J.E.; Turner, C.H. Molecular analysis of selective gas adsorption within composites of ionic polyimides and ionic liquids as gas separation membranes. *J. Chem. Phys.* **2019**, *516*, 71–83. [CrossRef]
14. Xue, C.; Feng, L.; Zhu, H.; Huang, R.; Wang, E.; Du, X.; Liu, G.; Hao, X.; Li, K. Pyridine-containing ionic liquids lowly loaded in large mesoporous silica and their rapid CO_2 gas adsorption at low partial pressure. *J. CO2 Utiliz.* **2019**, *34*, 282–292. [CrossRef]
15. Sun, X.; Luo, H.; Dai, S. Ionic liquids-based extraction: A promising strategy for the advanced nuclear fuel cycle. *Chem. Rev.* **2012**, *112*, 2100–2128. [CrossRef]
16. Azaceta, E.; Lutz, L.; Grimaud, A.; Vicent-Luna, J.M.; Hamad, S.; Yate, L.; Cabanero, G.; Grande, H.J.; Anta, J.A.; Tarascon, J.M.; et al. Electrochemical Reduction of Oxygen in Aprotic Ionic Liquids Containing Metal Cations: A Case Study on the Na-O_2 system. *Chem. Sus. Chem.* **2017**, *10*, 1616–1623. [CrossRef]
17. Vicent-Luna, J.M.; Azaceta, E.; Hamad, S.; Ortiz-Roldan, J.M.; Tena-Zaera, R.; Calero, S.; Anta, J.A. Molecular Dynamics Analysis of Charge Transport in Ionic-Liquid Electrolytes Containing Added Salt with Mono, Di, and Trivalent Metal Cations. *Chem. Phys. Chem.* **2018**, *19*, 1665–1673. [CrossRef]
18. Zhang, S.; Ueno, K.; Dokko, K.; Watanabe, M. Recent Advances in Electrolytes for Lithium-Sulfur Batteries. *Adv. Ener. Mat.* **2015**, *5*, 1500117. [CrossRef]
19. MacFarlane, D.R.; Tachikawa, N.; Forsyth, M.; Pringle, J.M.; Howlett, P.C.; Elliott, G.D.; Davis, J.H.; Watanabe, M.; Simon, P.; Angell, C.A. Energy applications of ionic liquids. *Energy Environ. Sci.* **2014**, *7*, 232–250. [CrossRef]
20. Sakhaeinia, H.; Jalili, A.H.; Taghikhani, V.; Safekordi, A.A. Solubility of H_2S in Ionic Liquids 1-Ethyl-3-methylimidazolium Hexafluorophosphate ([emim][PF_6]) and 1-Ethyl-3-methylimidazolium Bis(trifluoromethyl)sulfonylimide ([emim][Tf_2N]). *J. Chem. Eng.* **2010**, *55*, 5839–5845. [CrossRef]
21. Huang, K.; Cai, D.-N.; Chen, Y.-L.; Wu, Y.-T.; Hu, X.-B.; Zhang, Z.-B. Thermodynamic validation of 1-alkyl-3-methylimidazolium carboxylates as task-specific ionic liquids for H_2S absorption. *Am. Inst. Chem. Eng.* **2013**, *59*, 2227–2235. [CrossRef]
22. Castillo, J.M.; Vlugt, T.J.H.; Calero, S. Understanding Water Adsoprtion in Cu-BTC Metal-Organic Frameworks. *J. Phys. Chem. C* **2008**, *112*, 15934–15939. [CrossRef]
23. Devautour-Vinot, S.; Diaby, S.; da Cunha, D.; Serre, C.; Horcajada, P.; Maurin, G. Ligand Dynamics of Drug-Loaded Microporous Zirconium Terephthalates-Based Metal–Organic Frameworks: Impact of the Nature and Concentration of the Guest. *J. Phys. Chem. C* **2014**, *118*, 1983–1989. [CrossRef]
24. Gurdal, Y.; Keskin, S. Predicting Noble Gas Separation Performance of Metal Organic Frameworks Using Theoretical Correlations. *J. Phys. Chem. C* **2013**, *117*, 5229–5241. [CrossRef]
25. Li, J.R.; Sculley, J.; Zhou, H.C. Metal-organic frameworks for separations. *Chem. Rev.* **2012**, *112*, 869–932. [CrossRef] [PubMed]
26. Nasalevich, M.A.; van der Veen, M.; Kapteijn, F.; Gascon, J. Metal–organic frameworks as heterogeneous photocatalysts: Advantages and challenges. *Cryst. Eng. Comm.* **2014**, *16*, 4919–4926. [CrossRef]
27. Brandt, P.; Nuhnen, A.; Lange, M.; Mollmer, J.; Weingart, O.; Janiak, C. Metal-Organic Frameworks with Potential Application for SO_2 Separation and Flue Gas Desulfurization. *ACS Appl. Mater. Interfaces* **2019**, *11*, 17350–17358. [CrossRef]
28. Connolly, B.M.; Aragones-Anglada, M.; Gandara-Loe, J.; Danaf, N.A.; Lamb, D.C.; Mehta, J.P.; Vulpe, D.; Wuttke, S.; Silvestre-Albero, J.; Moghadam, P.Z.; et al. Tuning porosity in macroscopic monolithic metal-organic frameworks for exceptional natural gas storage. *Nat. Commun.* **2019**, *10*, 1–11. [CrossRef] [PubMed]
29. Dureckova, H.; Krykunov, M.; Aghaji, M.Z.; Woo, T.K. Robust Machine Learning Models for Predicting High CO_2 Working Capacity and CO_2/H_2 Selectivity of Gas Adsorption in Metal Organic Frameworks for Precombustion Carbon Capture. *J. Phys. Chem. C* **2019**, *123*, 4133–4139. [CrossRef]
30. Li, J.R.; Kuppler, R.J.; Zhou, H.C. Selective gas adsorption and separation in metal-organic frameworks. *Chem. Soc. Rev.* **2009**, *38*, 1477–1504. [CrossRef]
31. Makal, T.A.; Li, J.R.; Lu, W.; Zhou, H.C. Methane storage in advanced porous materials. *Chem. Soc. Rev.* **2012**, *41*, 7761–7779. [CrossRef] [PubMed]
32. Sumida, K.; Rogow, D.L.; Mason, J.A.; McDonald, T.M.; Bloch, E.D.; Herm, Z.R.; Bae, T.H.; Long, J.R. Carbon dioxide capture in metal-organic frameworks. *Chem. Rev.* **2012**, *112*, 724–781. [CrossRef] [PubMed]

33. Carlucci, L.; Ciani, G.; Maggini, S.; Proserpio, D.M.; Visconti, M. Heterometallic modular metal-organic 3D frameworks assembled via new tris-beta-diketonate metalloligands: Nanoporous materials for anion exchange and scaffolding of selected anionic guests. *Chemistry* **2010**, *16*, 12328–12341. [CrossRef]
34. Zhao, X.; Bu, X.; Wu, T.; Zheng, S.T.; Wang, L.; Feng, P. Selective anion exchange with nanogated isoreticular positive metal-organic frameworks. *Nat. Commun.* **2013**, *4*, 1–9. [CrossRef]
35. Furukawa, H.; Cordova, K.E.; O'Keeffe, M.; Yaghi, O.M. The chemistry and applications of metal-organic frameworks. *Science* **2013**, *341*, 1–12. [CrossRef] [PubMed]
36. Li, W. Metal–organic framework membranes: Production, modification, and applications. *Prog. Mat. Sci.* **2019**, *100*, 21–63. [CrossRef]
37. Theo, W.L.; Lim, J.S.; Hashim, H.; Mustaffa, A.A.; Ho, W.S. Review of pre-combustion capture and ionic liquid in carbon capture and storage. *App. Energy* **2016**, *183*, 1633–1663. [CrossRef]
38. Qiao, Z.; Wang, N.; Jiang, J.; Zhou, J.J.C.C. Design of amine-functionalized metal–organic frameworks for CO_2 separation: The more amine, the better? *Chem. Commun.* **2016**, *52*, 974–977. [CrossRef]
39. Zheng, X.-D.; Huang, Y.-L.; Tong, Y.-P.; Peng, C.-J. A 3D homochiral metal–organic framework with high selective adsorption property. *Inorg. Chem. Commun.* **2018**, *92*, 115–120. [CrossRef]
40. Abroshan, H.; Kim, H.J. On the structural stability of ionic liquid-IRMOF composites: A computational study. *Phys. Chem. Chem. Phys.* **2015**, *17*, 6248–6254. [CrossRef]
41. Gupta, K.M.; Chen, Y.; Hu, Z.; Jiang, J. Metal-organic framework supported ionic liquid membranes for CO2 capture: Anion effects. *Phys. Chem. Chem. Phys.* **2012**, *14*, 5785–5794. [CrossRef] [PubMed]
42. Li, Z.; Xiao, Y.; Xue, W.; Yang, Q.; Zhong, C. Ionic Liquid/Metal-Organic Framework Composites for H_2S Removal from Natural Gas: A Computational Exploration. *J. Phys. Chem. C.* **2015**, *119*, 3674–3683. [CrossRef]
43. Tranchemontagne, D.J.; Hunt, J.R.; Yaghi, O.M. Room temperature synthesis of metal-organic frameworks: MOF-5, MOF-74, MOF-177, MOF-199, and IRMOF-0. *Tetrahedron* **2008**, *64*, 8553–8557. [CrossRef]
44. Chen, Y.; Hu, Z.; Gupta, K.M.; Jiang, J. Ionic liquid/metal–organic framework composite for CO_2 capture: A computational investigation. *J. Phys. Chem. C* **2011**, *115*, 21736–21742. [CrossRef]
45. Bennett, C.H. Efficient Estimation of Free Energy Differences from Monte Carlo Data. *J. Comp. Phys.* **1976**, *22*, 245–268. [CrossRef]
46. Bruckner, S.; Boresch, S. Efficiency of alchemical free energy simulations. I. A practical comparison of the exponential formula, thermodynamic integration, and Bennett's acceptance ratio method. *J. Comp. Chem.* **2011**, *32*, 1303–1319. [CrossRef]
47. Tian, Z.; Dai, S.; Jiang, D.-E. Confined Ionic Liquid in an Ionic Porous Aromatic Framework for Gas Separation. *ACS Appl. Poly. Mater.* **2018**, *1*, 95–102. [CrossRef]
48. Burtch, N.C.; Jasuja, H.; Walton, K.S. Water stability and adsorption in metal-organic frameworks. *Chem. Rev.* **2014**, *114*, 10575–10612. [CrossRef] [PubMed]
49. Amhamed, A.; Atilhan, M.; Berdiyorov, G. Permeabilities of CO_2, H_2S and CH_4 through Choline-Based Ionic Liquids: Atomistic-Scale Simulations. *Molecules* **2019**, *24*, 14. [CrossRef]
50. Vicent-Luna, J.M.; Gutiérrez-Sevillano, J.J.; Anta, J.A.; Calero, S. Effect of Room-Temperature Ionic Liquids on CO_2 Separation by a Cu-BTC Metal–Organic Framework. *J. Phys. Chem. C* **2013**, *117*, 20762–20768. [CrossRef]
51. Ramdin, M.; Balaji, S.P.; Torres-Knoop, A.; Dubbeldam, D.; de Loos, T.W.; Vlugt, T.J.H. Solubility of Natural Gas Species in Ionic Liquids and Commercial Solvents: Experiments and Monte Carlo Simulations. *J. Chem. Eng. Data* **2015**, *60*, 3039–3045. [CrossRef]
52. Jalili, A.H.; Shokouhi, M.; Maurer, G.; Zoghi, A.T.; Sadeghzah Ahari, J.; Forsat, K. Measuring and modelling the absorption and volumetric properties of CO_2 and H_2S in the ionic liquid 1-ethyl-3-methylimidazolium tetrafluoroborate. *J. Chem. Thermo.* **2019**, *131*, 544–556. [CrossRef]
53. Anthony, J.L.; Anderson, J.L.; Maginn, E.J.; Brennecke, J.F. Anion Effects on Gas Solubility in Ionic Liquids. *J. Phys. Chem. B* **2005**, *109*, 6366–6374. [CrossRef] [PubMed]
54. Cauliez, P.; Polo, V.; Roisnel, T.; Llusar, R.; Fourmigué, M. The thiocyanate anion as a polydentate halogen bond acceptor. *Cryst. Eng. Comm.* **2010**, *12*, 558–566. [CrossRef]
55. Santiago, R.; Lemus, J.; Outomuro, A.X.; Bedia, J.; Palomar, J. Assessment of ionic liquids as H_2S physical absorbents by thermodynamic and kinetic analysis based on process simulation. *Sep. Purif. Technol.* **2019**, *233*, 116050. [CrossRef]

56. Kim, Y.S.; Choi, W.Y.; Jang, J.H.; Yoo, K.P.; Lee, C.S. Solubility measurement and prediction of carbon dioxide in ionic liquids. *Fluid Phase Equilibria* **2005**, *228–229*, 439–445. [CrossRef]
57. Zhou, L.; Fan, J.; Shang, X. CO(2) Capture and Separation Properties in the Ionic Liquid 1-n-Butyl-3-Methylimidazolium Nonafluorobutylsulfonate. *Materials* **2014**, *7*, 3867–3880. [CrossRef]